

Impact of the TCO Microstructure on the Electronic Properties of Carbazole-Based Self-Assembled Monolayers

Suzana Kralj,* Pia Dally, Pantelis Bampoulis, Badri Vishal, Stefaan De Wolf, and Monica Morales-Masis*



Cite This: ACS Materials Lett. 2024, 6, 366–374



Read Online

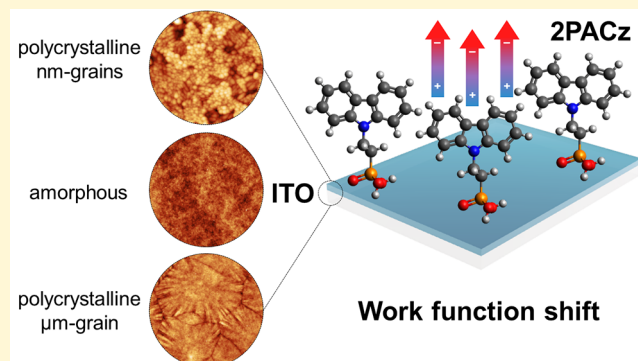
ACCESS |

Metrics & More

Article Recommendations

Supporting Information

ABSTRACT: Carbazole-based self-assembled monolayers (PACz-SAMs), anchored via their phosphonic acid group on a transparent conductive oxide (TCO), have demonstrated excellent performance as hole-selective layers in perovskite/silicon tandem solar cells. Yet, whereas different PACz-SAMs have been explored, the role of the TCO, and specifically its microstructure, on the hole transport properties of the TCO/PACz-SAMs stack has been largely overlooked. Here, we demonstrate that the TCO microstructure directly impacts the work function (WF) shift after SAM anchoring and is responsible for WF variations at the micro/nanoscale. Specifically, we studied Sn-doped In_2O_3 (ITO) substrates with amorphous and polycrystalline (featuring either nanoscale- or microscale-sized grains) microstructures before and after 2PACz-SAMs and $\text{NiO}_x/2\text{PACz}$ -SAMs anchoring. With this, we established a direct correlation between the ITO crystal grain orientation and 2PACz-SAMs local potential distribution, i.e., the WF. Importantly, these variations vanish for amorphous oxides (either in the form of amorphous ITO or when adding an amorphous NiO_x buffer layer), where a homogeneous surface potential distribution is found. These findings highlight the importance of TCO microstructure tuning, to enable both high mobility and broadband transparent electrodes while ensuring uniform WF distribution upon application of hole transport SAMs, both critical for enhanced device performance.



Transparent conductive oxides (TCOs) are omnipresent in a range of high-efficiency optoelectronic devices, including perovskite solar cells (PSCs), both in their single-junction and tandem implementations.^{1,2} Among the various available TCOs, indium tin oxide (ITO) remains a common choice as a transparent electrode for optoelectronic applications as it is well established and scalable, and commercial glass/ITO substrates are readily available. However, further progress in PSC performance could benefit from additional TCO optimization, for instance, by enhancing the transparency/conductivity trade-off. Moreover, with the rise of monolithic perovskite/perovskite and perovskite/silicon tandem solar cells, TCOs are also often used as an interband recombination junction³ deposited onto the bottom cell (i.e., a perovskite or silicon cell), connecting the subcells in series. Both in the single-junction and tandem cases for inverted *p-i-n* devices, the hole transport layer (HTL) is deposited onto the TCO, followed by the perovskite absorber and the electron selective contact stack. Depending on the TCO deposition method and process conditions, different

microstructures can be achieved which may also influence the optoelectronic properties. For instance, amorphous TCOs generally feature a narrower band gap as compared to polycrystalline TCOs due to their distorted absorption edge.^{4,5} The electron mobility in TCOs can also be influenced by the microstructure, with typically high mobilities achieved for polycrystalline TCOs with large grains.^{5–9}

For the case of HTLs for inverted PSCs, self-assembled monolayers (SAMs), such as carbazole-based with a phosphonic acid anchoring group (PACz-SAMs), have attracted much attention in recent years.^{10–12} These SAMs shift the work function of the TCO substrate to higher values due to the interfacial dipole they introduce, enhancing the hole

Received: September 28, 2023

Revised: November 30, 2023

Accepted: November 30, 2023

Published: December 26, 2023



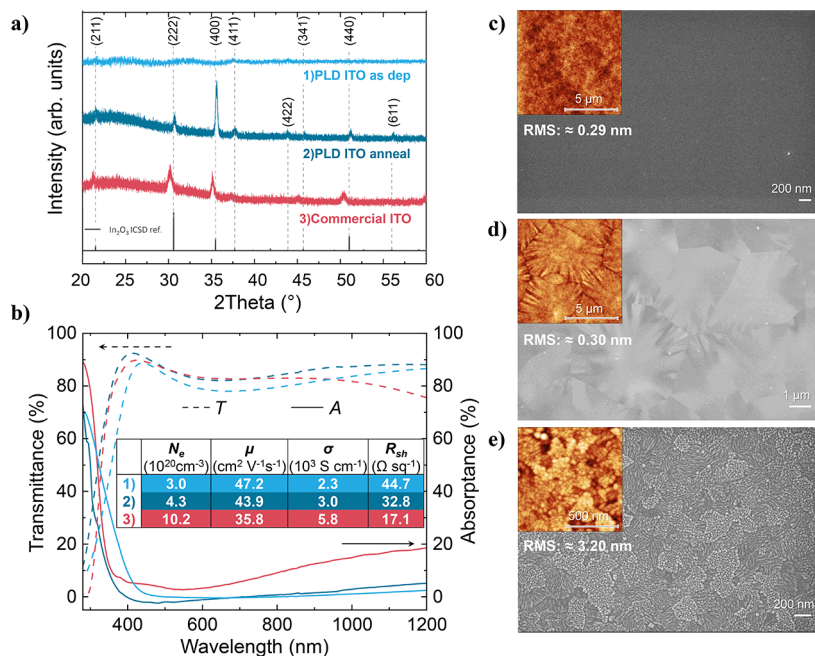


Figure 1. (a) X-ray diffractogram; (b) Optical and electrical properties of studied ITOs. SEM top-view images with an AFM topography inset and RMS values for (c) PLD ITO as deposited; (d) PLD ITO annealed; and (e) Commercial ITO. The thickness of all films is ≈ 100 nm.

selectivity of the contact.^{12–14} So far, the TCO/PACz-SAMs stack has gained particular attention as a hole selective contact for inverted perovskite,^{15–21} organic,^{22,23} perovskite/organic,²⁴ perovskite/perovskite,^{25–27} and recent record perovskite/silicon tandem solar cells^{28,29} where often they have been found to result in superior passivation of the HTL/photoabsorber interface, a fast hole extraction rate, and minimal parasitic absorption.³⁰ On the downside, the presence of imperfections in PACz-SAMs coatings on polycrystalline TCO is frequently reported,^{30–33} preventing optimal device performance and stability. So far, addressing this challenge has primarily involved either blending SAM molecules of varying sizes to ensure high packing density^{26,34–37} or anchoring the PACz-SAMs to a hole-selective metal-oxide buffer layer, such as nickel oxide (NiO_x).^{32,38–40} The effect of the TCO substrate surface properties, such as roughness, morphology, and composition, on the quality of phosphonic acid-based SAMs has been studied before.^{41–43} However, to the best of our knowledge, no comprehensive investigation into the correlation between the microstructure of TCOs, specifically the grain orientation, and the hole transporting properties of TCO/PACz-SAMs stacks has been reported. To elucidate this, herein, we study the effect of 2PACz, [2-(9H-carbazol-9-yl)ethyl]phosphonic acid (Figure S1), a commonly used SAM hole selective contact, on the WF shifts of various ITO substrates. Furthermore, we investigate the potential distribution and its link to the WF along the surface of distinct types of ITO substrates with different microstructures. In this work, we focus on ITO as a model system, but the conclusions are valid for other TCOs. Specifically, we studied ITO substrates with comparable sheet resistance but distinct microstructures, namely: commercial ITO, featuring a polycrystalline microstructure with small (nm-scale) grains, and pulsed laser deposited (PLD) ITO, either amorphous or polycrystalline with large (μm -scale) grains. Moreover, the effect of introducing a sputtered NiO_x layer between the different ITO electrodes and 2PACz-SAMs was analyzed. The potential

distribution was mapped by using Kelvin probe force microscopy (KPFM), while the grain orientation of the ITO for the same area was measured by electron backscatter diffraction (EBSD) analysis. Ultraviolet photoelectron spectroscopy (UPS) was used to determine absolute WF values and verify the values determined by KPFM. Based on these experiments, we demonstrate how the ITO crystalline grain orientation and grain size influence the potential distribution in the ITO/2PACz-SAMs electrodes, compare the WF values achieved for the distinct ITOs, and discuss the role of a NiO_x buffer layer on achieving a uniform potential distribution for hole extraction. These insights are invaluable for advancing solar cells and other optoelectronic device designs, ultimately leading to improvements in the efficiency, stability, and reliability.

EXPERIMENTAL SECTION

100 nm Sn-doped In_2O_3 (10/90 wt % $\text{SnO}_2/\text{In}_2\text{O}_3$) thin-films with sheet resistance (R_{sh}) below $50 \Omega/\text{sq}$, representing typical TCO device requirements, with three different microstructures were selected for this study. The ITO films were deposited on glass substrates by PLD at room temperature. As-deposited ITO films were found to be amorphous; subsequent annealing for 20 min at 450°C (Figure S2) resulted in a polycrystalline structure, as confirmed by XRD (Figure 1a, Table S1). Top-view SEM and AFM scans (Figure 1c-d) show a flat, featureless surface for the amorphous ITO (RMS of 0.29 nm) and large micrometer-sized grains for the annealed ITO films (RMS of 0.30 nm). This observed change in crystallinity and microstructure is due to a solid phase crystallization, as previously reported for sputtered In-based TCOs.^{7,8} In the process of physical vapor deposition of In-based TCOs at room temperature (by either PLD or sputtering), nanocrystals are generated within an amorphous matrix. These nanocrystals act as nucleation sites, facilitating the growth of grains during a subsequent annealing step.⁷ Commercially available ITO substrates (Ossila Ltd.), featuring a polycrystalline structure

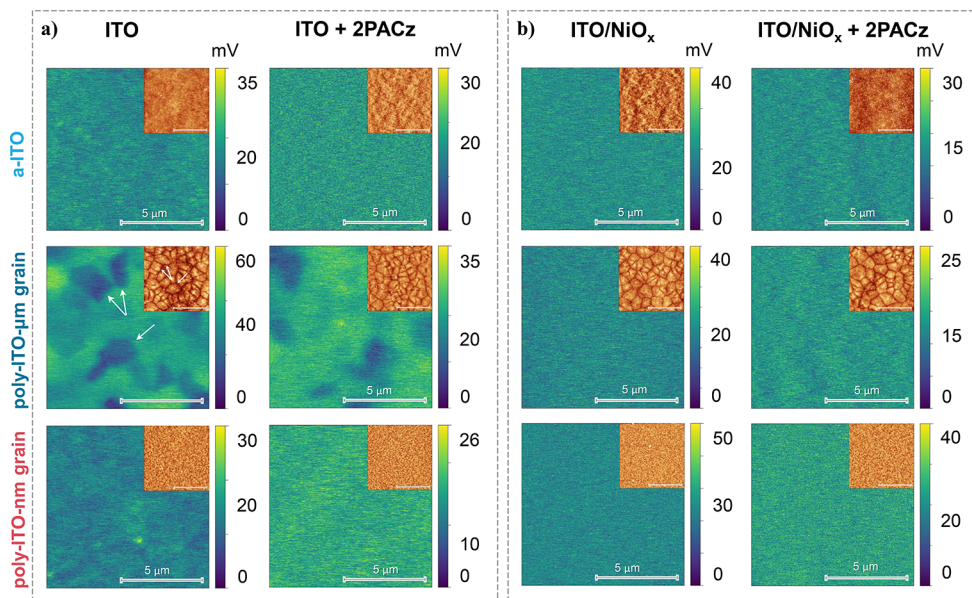


Figure 2. KPFM mapping for the stacks: (a) ITO with and without 2PACz-SAMs; (b) ITO/ NiO_x with and without 2PACz-SAMs (scanning area $10 \times 10 \mu\text{m}^2$, larger image: CPD mapping; inset: topography. Note: To ensure a precise depiction of CPD values for each sample, the color scale bar has been adjusted to accommodate the observed deviations. The scale bar of all images, including insets, is equivalent to 5 μm .).

and nanoscale grains microstructure (RMS of 3.20 nm), as depicted in Figure 1a and e, respectively, were used to compare the influence of the grain size in the WF distribution. Figure S3 showcases the comparison of three commercially available ITO substrates from different suppliers. The data indicate that while the optical and electrical properties are within the same range for the three commercial ITOs, there is a slight difference in the surface morphology and roughness. Mainly, the thicker ITO (from supplier 3) shows slight variations in grain distribution and height, which could affect the quality of the SAMs coating.^{41,42} This minor differences in roughness could lead to lab-to-lab reproducibility of the quality of SAMs. Nevertheless, for the purposes of this study and based on the proximity on the ITO properties, we have selected one representative commercial ITO (supplier 1).

All studied ITO films demonstrate >80% transmittance in the wavelength range of 350–750 nm (Figure 1b). For wavelengths above 750 nm, the commercial ITO samples exhibited a larger absorption (>15%) as compared to PLD ITO. This can be explained by free carrier absorption as the concentration of free carriers, N_e , is significantly higher ($10 \times 10^{20} \text{ cm}^{-3}$) for commercial ITO films as compared to PLD films (up to $4.5 \times 10^{20} \text{ cm}^{-3}$). The electrical properties of the ITO films determined from Hall effect measurements in the van der Pauw configuration are summarized in the inset of Figure 1b. Additionally, an increase in the optical band gap for PLD ITO annealed films from ~ 3.4 eV for as-deposited ITO to ~ 3.7 eV for annealed ITO was estimated from the Tauc plot in Figure S4.

For conciseness, as-deposited ITO films will further be referred to as “*a-ITO*”, annealed ITO polycrystalline films with large (μm -sized) grains will further be referred to as “*poly-ITO-μm-grain*”, and commercial ITO polycrystalline films with small (nm-sized) grains will further be referred to as “*poly-ITO-nm-grain*”.

To gain insight into the surface potential distribution of the ITO films with distinct microstructural properties, KPFM was

performed, which directly maps the contact potential difference (CPD) between a conducting AFM tip and the sample (Figure S5). Here, a relatively large area of $10 \times 10 \mu\text{m}^2$ was scanned. The resulting CPD maps and the corresponding topography image (inset) are shown in the left column of Figure 2a. In the case of *a-ITO* and *poly-ITO-nm-grains*, a relatively consistent surface potential across the scanned film area is measured, indicating an overall homogeneous WF distribution. However, in the case of *poly-ITO-μm-grain* films, the CPD is not uniform across the scanned area, as observed by the lighter and darker domains in Figure 2a, representing areas of higher and lower WF values, respectively. The domains match the corresponding large grains in the topography inset, as marked with white arrows.

Subsequently, 2PACz-SAMs were deposited onto the three ITO films described above (details in the SI). The right column in Figure 2a displays the CPD maps, accompanied by insets of topographic AFM images of the ITO/2PACz-SAMs substrates. Generally, the topography remained virtually unaltered with the introduction of 2PACz-SAMs, but a systematic overall reduction in CPD confirms the presence of 2PACz-SAMs on the surface and implies an increase in the WF. Notably, in the case of the *poly-ITO-μm-grain* films, the presence of domains with distinct CPD values remains even after the 2PACz-SAMs application. For the *poly-ITO-μm* grain films, a narrowing of the CPD-distribution is observed. We hypothesized that this can be a combined effect of the UV–O₃ plasma treatment before the application of SAMs which ensures an oxygen terminated surface (and a hydroxyl-rich surface upon exposure to ambient air) and by a quenching effect, which is related to the interaction dynamics between the tip, the surface, and the 2PACz molecules as explained in the SI and Figure S6.

NiO_x is a p-type, high work function metal oxide with good transparency and has been demonstrated as an effective hole transport layer in inverted PSCs, deposited through a variety of methods, including sputtering.^{44,45} However, it is widely

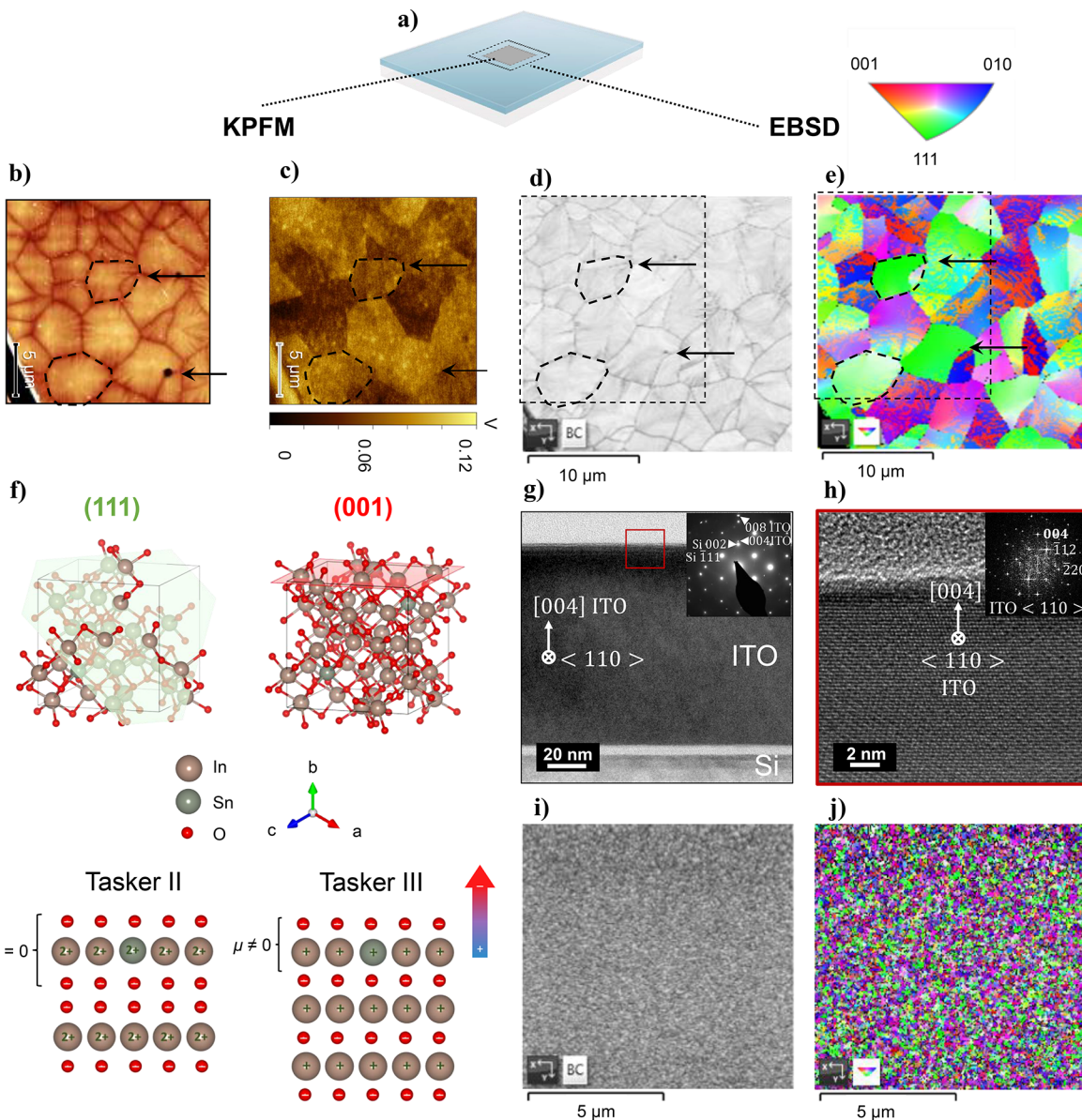


Figure 3. Grain orientation influence on the local WF. (a) Schematic representation of the point of interest (POI) on the sample; (b) topography and (c) CPD mapping from KPFM measurements; (d) SEM image and (e) EBSD mapping of the poly-ITO- μm -grain ITO film; (f) representation of (001) and (111) plane orientations for ITO and analogous Tasker surfaces; (g) cross-sectional TEM image and SAEDP (inset) of the poly-ITO- μm -grain film and (h) HR-TEM and the corresponding fast-Fourier-transform (FFT) (inset) image of the top surface showing preferential surface termination in 4×(001) orientation; (i) SEM image and (j) EBSD mapping of the poly-ITO-nm grain ITO film (The black dashed square in d-e represents the area on which both KPFM and EBSD were performed. Arrows and dash-framed grains serve as guiding marks.).

reported that its direct contact with the perovskite absorber leads to a defective interface, leading to the development of several NiO_x surface passivation approaches, including the use of PACz-SAMs.^{32,46,47} While similar performances have been reported for PSCs with ITO/2PACz-SAMs and ITO/ NiO_x /2PACz-SAMs, it has been proposed^{40,47} that the use of a thin NiO_x buffer layer deposited on top of ITO helps to homogenize morphological and energetical differences on the ITO substrates, enabling higher reproducibility in devices for the ITO/ NiO_x /2PACz-SAMs stack as compared to the ITO/2PACz-SAMs counterpart.^{32,39} It is hypothesized that the presence of a NiO_x buffer layer offers a dual function. First, it acts as a barrier, preventing a direct contact between the perovskite layer and the TCO in the case of pinhole formation

within the PACz-SAM layer. Simultaneously, in the event of pinhole formation, the NiO_x hole-selective nature enables efficient charge carrier extraction, mitigating potential adverse effects. Furthermore, it enhances substrate surface properties, improving PACz-SAMs coverage.^{32,38,40,42} Most of the reported NiO_x hole transport layers are either amorphous or nanocrystalline, with randomly oriented nanometer-sized grains. We suggest that this amorphous or nanocrystalline microstructure is also beneficial for homogenizing the surface roughness and the surface potential.

To confirm this, here, we sputtered an amorphous NiO_x layer (14 nm) onto the studied ITOs. Figure S7 displays a featureless X-ray diffraction pattern, confirming the formation of an amorphous NiO_x film. For elaborate characterizations

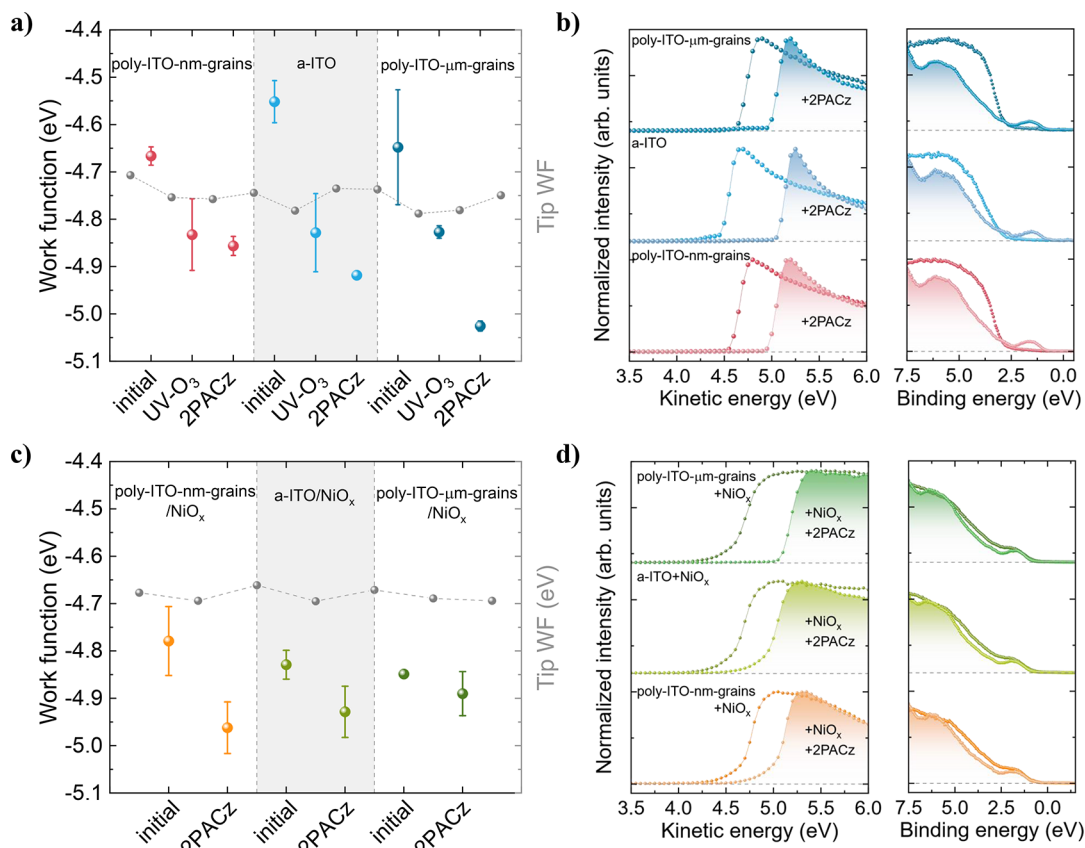


Figure 4. KPFM WF values (a, c), UPS secondary electron cutoff (SECO) and valence band region (b, d) for ITO with and without 2PACz (a, b) and ITO/NiO_x with and without 2PACz (c, d). (The tip WF is presented in (a, c) for reference.)

and properties of the NiO_x layer, we refer the reader to ref 44. We note that NiO_x subsequently underwent a treatment with a potassium chloride (KCl) solution to passivate its surface defects.⁴⁸ Topography and surface potential images for the resulting ITO/NiO_x stack with and without 2PACz-SAMs are shown in Figure 2b. The left column illustrates CPD mappings and topography insets for the ITO/NiO_x configuration. AFM images reveal that the NiO_x layer follows the topological features of the distinct ITO substrates. However, the presence of NiO_x on the surfaces of the ITO films clearly reduces the variations in the CPD values along the surfaces of all ITOs. Consequently, a uniform surface potential distribution emerges, regardless of the underlying microstructure of the ITO. This underscores the efficacy of utilizing an amorphous NiO_x buffer layer as a surface modifier, effectively countering potential nonuniformities, and promoting uniform electronic response in the films, particularly in the case of *poly-ITO-μm-grain* films.

Following KCl-treated NiO_x 2PACz-SAMs were deposited on ITO/NiO_x substrates (Figure 2b, right column). Figures S12 and S13 and text within the SI further demonstrate that remaining KCl crystals on the NiO_x surface after the KCl treatment are washed away after the 2PACz-SAMs deposition. With the incorporation of 2PACz-SAMs, the uniform CPD was preserved for all of the studied ITOs/NiO_x, but the lower CPD values (as compared to the case of ITO/NiO_x alone) serve as evidence of the presence of 2PACz on the surface, also indicating a WF increase. The WF values were later confirmed by UPS (Figure 4). We argue that the enhancement in CPD uniformity achieved by introducing a NiO_x layer on top of ITO

before 2PACz anchoring is the outcome of a synergistic interplay among its amorphous nature (i.e., nonpreferred crystal orientation) and increased hydroxyl group concentration, rather than their individual contributions as previously reported.^{40,42,49}

Colocalization KPFM and EBSD Mapping: Correlating ITO Grain Orientation with Work Function. The KPFM findings reveal a notable correspondence between the CPD domains and the respective ITO grains in the *poly-ITO-μm-grain* films. To ascertain whether the identified domains originate from distinct crystalline orientations, a combined approach employing EBSD mapping and KPFM measurements is adopted for simultaneous topographical, electronic, and microstructural imaging of the ITO surface on the same point of interest (POI). This is schematically represented in Figure 3a (details on the protocol procedure⁵⁰ in the SI).

It is well-established that crystal orientations can lead to diverse atomic arrangements on a material's surface, influencing the electronic structure and impacting the WF. It has been proposed that generally, closely packed planes (high atomic density) display higher WF compared to loosely packed planes (low atomic density).⁵¹ From reported surface densities based on density functional theory calculations for In₂O₃ (100) > (110) > (111), it is speculated that ITO (100) planes possess higher WF.⁵² Another theory that may elucidate the phenomenon of crystalline orientation's influence on local WF variation is the surface polarity concept, introduced by Tasker.⁵³ While the initial observations were for In₂O₃,^{52,54,55} this concept can be extended to ITO. In detail, the (111) plane is a Tasker II type of surface without surface dipole

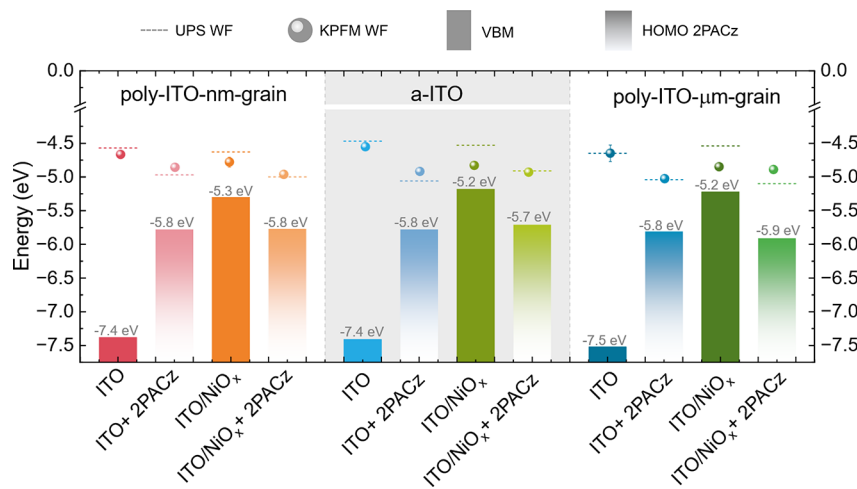


Figure 5. Overview of UPS and KPFM data and reconstructed energy level diagram for the distinct stacks studied (Spheres and dashed lines represent work function values determined by KPFM and UPS, respectively; gray numbers refer to ionization potential, I_p , which corresponds to VBM or HOMO values for TCOs and the TCO/2PACz stack, respectively.).

perpendicular to the surface normal. On the other hand, the (100) plane corresponds to a Tasker III type of surface, characterized by alternating charged planes that lead to a dipolar moment on the uppermost surface layer pointing away from the surface in the normal direction. Consequently, this induced surface dipole makes the removal of an electron more challenging, resulting in an increased WF¹⁴ (Figure 3f).

Topography and CPD maps obtained from KPFM for *poly-ITO-μm-grain* films are presented in Figure 3b-c. Using the dash-framed grains and arrows as guiding marks, we note that the indicated grains exhibit a lighter coloration, implying a higher applied CPD and thus a lower WF. The respective grains in the EBSD map (out-of-plane, z-direction) are colored green, indicating (111) orientation (Figure 3d-e, S8). Conversely, the darker-colored grains identified on the CPD map, reflecting a low applied CPD, thus a high WF, align with the red/blue colored grains on the EBSD map, which correspond to the (001) family of planes. The preferred surface termination of a single grain along 4 × (001) was also confirmed with high-resolution transmission electron microscopy (HR-TEM) and selected area diffraction pattern (SADP) as presented in Figure 3g-h.

Furthermore, we conducted EBSD on *poly-ITO-nm-grain* films, as shown in Figure 3i-j and Figure S9. The distinct crystal orientations of the nanometer-scale grains are visible, suggesting that local WF variations induced by the grain's orientation could also be expected. However, due to the nanometer-scale of the grains, the spatial resolution of the KPFM tip was not sufficient to detect such nanoscale variation. Despite this, it is suggested that local WF variations, even at the nanoscale, are expected on any polycrystalline sample.^{S1,55} The presence of significant energetic variations across a material can lead to unwanted effects on a device level, such as an uneven charge distribution, altered electronic transport properties, and even limitations in device efficiency and performance as previously reported.^{32,38,43}

To verify the WF values determined by KPFM and to extract the valence band maximum (VBM) and highest occupied molecular orbital (HOMO) levels, UPS measurements were conducted. Figure 4a showcases the WF values determined by KPFM for the studied ITOs, in their initial state (right upon solvent cleaning procedure), after UV–O₃ treatment and

subsequent 2PACz-SAMs deposition. The large error bar for the *poly-ITO-μm-grain* film could be ascribed to the presence of the distinct crystalline grain orientations. However, the overall WF of all bare ITOs is found within the same range, and a systematic increase in the WF after UV–O₃ treatment and upon 2PACz-SAMs anchoring is evident across all studied ITO films. This trend is expected, as any form of surface treatment inherently alters the surface potential and thereby impacts the WF.^{S1}

UPS results complement these findings, indicating a pronounced shift of the secondary electron cutoff (SECO) toward lower binding energies. This shift strongly implies a substantial WF increase upon the anchoring of 2PACz-SAMs, a phenomenon consistent across all of the examined cases. In addition, the VBM region spectra show a significant modification after 2PACz-SAMs deposition. Specifically, the characteristic sharp, linear-like form typical of TCOs—attributed to localized electronic states—changes to a hump-like HOMO edge, characteristic of organic molecules with delocalized π -electrons⁵⁶ (Figure 4b). The presence of 2PACz-SAMs on the surface was further confirmed via X-ray photoelectron spectroscopy (XPS) analysis (Figures S10–S11).

As observed in Figure 2b (left column), the introduction of an amorphous NiO_x layer appears to mitigate surface potential disparities arising from the distinct microstructures of the ITO films. Measuring the average WF values by KPFM and UPS, only a slight variation in the WF is observed for the different ITOs after NiO_x and NiO_x/2PACz-SAMs deposition (Figure 4c-d).

The reconstructed energy level diagram represented in Figure 5 shows the values of the work function determined by KPFM (sphere) and UPS (dashed line) and ionization potential, I_p (numerical values in gray font). All values are listed in Table S2. An overall good correlation between two independent techniques (each operating at different conditions, i.e., UPS at ultrahigh vacuum and KPFM at ambient air) and a consistent trend in the WF increase upon ITO surface modification can be observed (for a detailed explanation, check Figures S12 and S13).

As expected, all three ITO films have a pronounced n-type character as their Fermi level is far from VBM. Modified ITOs,

either with 2PACz-SAMs or NiO_x only, or a combination $\text{NiO}_x/2\text{PACz}$ -SAMs shifted the Fermi level closer to the ionization potential level (HOMO or VBM, respectively), indicating the p-type characteristics and enhanced hole selectivity. It is worth highlighting that the values of the WF and VBM for ITO/ NiO_x agree with previously reported values for ALD deposited NiO_x (4.6–4.7 and 5.3 eV, respectively).³² Upon depositing 2PACz-SAMs, the WF is further increased, due to the molecular dipole moment that 2PACz-SAMs introduce,⁴⁷ contributing to the surface energy term.⁵¹ Notably, the WF values for the ITO/2PACz-SAMs and ITO/ $\text{NiO}_x/2\text{PACz}$ -SAMs cases are quite similar. Going back to the KPFM mapping, we suggest that the main advantage of NiO_x in addition to its hole transport properties is its amorphous nature, minimizing pinhole formation and ensuring a uniform WF distribution due to the lack of preferential grain orientation. We therefore argue that the use of an amorphous metal oxide with adequate WF for hole (or electron) extraction or an amorphous TCO buffer layer ensures an enhanced coverage of the 2PACz-SAMs and, with it, a uniform WF distribution. This combination holds the potential to improve energy level alignment and charge extraction on a device scale, thereby enhancing the overall device performance, reproducibility, and stability.

In summary, we studied the impact of the ITO microstructure on the electronic properties of hole-selective transport layers NiO_x and 2PACz-SAMs. Three different types of ITO thin-films morphology and microstructure were characterized. Correlated KPFM and EBSD mapping revealed that polycrystalline ITO films present a nonuniform distribution of the surface potential, subsequently impacting WF uniformity. The application of 2PACz-SAMs was not sufficient to overcome the lateral inhomogeneity in the WF inherent to the polycrystalline ITO films. However, we found that this challenge can be successfully addressed by employing either an amorphous TCO or an amorphous NiO_x buffer layer, where there is no preferential grain orientation, and low surface roughness is ensured. In the context of applying TCOs and PACz-SAMs in solar cells, e.g., in perovskite/silicon tandems, polycrystalline TCOs offer attractive properties, such as high mobility and minimum parasitic absorption losses from the visible to the near-infrared wavelengths. To overcome the nonhomogenous WF distribution upon hole transport SAMs anchoring on polycrystalline TCOs, an amorphous buffer layer (or surface modification) is recommended to ensure a uniform potential distribution and minimum nonradiative losses at the perovskite/HTL interface, ultimately improving either the device performance or reducing device-to-device variations.

■ ASSOCIATED CONTENT

SI Supporting Information

The Supporting Information is available free of charge at <https://pubs.acs.org/doi/10.1021/acsmaterialslett.3c01166>.

Detailed description of used materials, applied experimental methods and procedures; elaborated XRD data, annealing series data, Tauc plot, KPFM and UPS WF values in tabular format, KPFM maps of ITO/ NiO_x KCl treated surface, XPS survey spectra, EBSD analysis ([PDF](#))

■ AUTHOR INFORMATION

Corresponding Authors

Suzana Kralj – MESA+ Institute for Nanotechnology, University of Twente, Enschede 7500 AE, The Netherlands;  orcid.org/0000-0003-2847-8359; Email: s.k.kralj@utwente.nl

Monica Morales-Masis – MESA+ Institute for Nanotechnology, University of Twente, Enschede 7500 AE, The Netherlands;  orcid.org/0000-0003-0390-6839; Email: m.moralesmasis@utwente.nl

Authors

Pia Dally – KAUST Solar Center (KSC), Physical Sciences and Engineering Division (PSE), King Abdullah University of Science and Technology (KAUST), Thuwal 23955-6900, Kingdom of Saudi Arabia

Pantelis Bampoulis – Physics of Interfaces and Nanomaterials, MESA+ Institute for Nanotechnology, University of Twente, Enschede 7500 AE, The Netherlands;  orcid.org/0000-0002-2347-5223

Badri Vishal – KAUST Solar Center (KSC), Physical Sciences and Engineering Division (PSE), King Abdullah University of Science and Technology (KAUST), Thuwal 23955-6900, Kingdom of Saudi Arabia

Stefaan De Wolf – KAUST Solar Center (KSC), Physical Sciences and Engineering Division (PSE), King Abdullah University of Science and Technology (KAUST), Thuwal 23955-6900, Kingdom of Saudi Arabia;  orcid.org/0000-0003-1619-9061

Complete contact information is available at:
<https://pubs.acs.org/10.1021/acsmaterialslett.3c01166>

Author Contributions

CRedit: Suzana Kralj conceptualization, data curation, formal analysis, investigation, visualization, writing-original draft, writing-review & editing; Pia Dally formal analysis, investigation, writing-review & editing; Pantelis Bampoulis methodology, resources, writing-review & editing; Badri Vishal investigation, visualization, writing-review & editing; Stefaan De Wolf project administration, resources, writing-review & editing; Monica Morales-Masis conceptualization, funding acquisition, methodology, project administration, supervision, writing-review & editing.

Notes

The authors declare no competing financial interest.

■ ACKNOWLEDGMENTS

This project is financed by the European Research Council (ERC) under the European Union's Horizon 2020 Research and Innovation Program (CREATE, Grant Agreement No. 852722). The authors would like to acknowledge P.-A. Repecaud and Y. Smirnov for input information on PLD depositions, M. Smithers for SEM and EBSD imaging, D. M. Cunha, R. Saive, L. Chen, and P. De Wolf for discussions on AFM and KPFM measurements, A. A. Said for guidance on NiO_x sputtering, and E. Aydin for fruitful discussions on ITO/2PACz properties.

■ REFERENCES

- (1) Morales-Masis, M.; De Wolf, S.; Woods-Robinson, R.; Ager, J. W.; Ballif, C. Transparent Electrodes for Efficient Optoelectronics. *Adv. Electron. Mater.* **2017**, 3 (5), 1600529.

- (2) Fortunato, E.; Ginley, D.; Hosono, H.; Paine, D. C. Transparent Conducting Oxides for Photovoltaics. *MRS Bull.* **2007**, *32* (3), 242–247.
- (3) De Bastiani, M.; Subbiah, A. S.; Aydin, E.; Isikgor, F. H.; Allen, T. G.; De Wolf, S. Recombination Junctions for Efficient Monolithic Perovskite-Based Tandem Solar Cells: Physical Principles, Properties, Processing and Prospects. *Mater. Horiz.* **2020**, *7* (11), 2791–2809.
- (4) Walsh, A.; Da Silva, J. L. F.; Wei, S.-H. Interplay between Order and Disorder in the High Performance of Amorphous Transparent Conducting Oxides. *Chem. Mater.* **2009**, *21* (21), 5119–5124.
- (5) Kim, J.; Shrestha, S.; Souris, M.; Connell, J. G.; Park, S.; Seo, A. High-Temperature Optical Properties of Indium Tin Oxide Thin-Films. *Sci. Rep.* **2020**, *10* (1), 12486.
- (6) Aydin, E.; De Bastiani, M.; Yang, X.; Sajjad, M.; Aljamaan, F.; Smirnov, Y.; Hedhili, M. N.; Liu, W.; Allen, T. G.; Xu, L.; Van Kerschaver, E.; Morales-Masis, M.; Schwingenschlögl, U.; De Wolf, S. Zr-Doped Indium Oxide (IZRO) Transparent Electrodes for Perovskite-Based Tandem Solar Cells. *Adv. Funct. Mater.* **2019**, *29* (25), 1901741.
- (7) Dzhigaev, D.; Smirnov, Y.; Repecaud, P.-A.; Marçal, L. A. B.; Fevola, G.; Sheyfer, D.; Jeangros, Q.; Cha, W.; Harder, R.; Mikkelsen, A.; Wallentin, J.; Morales-Masis, M.; Stuckelberger, M. E. Three-Dimensional In Situ Imaging of Single-Grain Growth in Polycrystalline $\text{In}_2\text{O}_3:\text{Zr}$ Films. *Commun. Mater.* **2022**, *3* (1), 38.
- (8) Rucavado, E.; Landucci, F.; Dobeli, M.; Jeangros, Q.; Boccard, M.; Hessler-Wyser, A.; Ballif, C.; Morales-Masis, M. Zr-doped Indium Oxide Electrodes: Annealing and Thickness Effects on Microstructure and Carrier Transport. *Phys. Rev. Mater.* **2019**, *3* (8), 084608.
- (9) Smirnov, Y.; Schmengler, L.; Kuik, R.; Repecaud, P. A.; Najafi, M.; Zhang, D.; Theelen, M.; Aydin, E.; Veenstra, S.; De Wolf, S.; Morales-Masis, M. Scalable Pulsed Laser Deposition of Transparent Rear Electrode for Perovskite Solar Cells. *Adv. Mater. Technol.* **2021**, *6* (2), 2000856.
- (10) Wang, S.; Guo, H.; Wu, Y. Advantages and Challenges of Self-Assembled Monolayer as a Hole-Selective Contact for Perovskite Solar Cells. *Mater. Futures* **2023**, *2* (1), 012105.
- (11) Jiang, W.; Li, F.; Li, M.; Qi, F.; Lin, F. R.; Jen, A. K. pi-Expanded Carbazoles as Hole-Selective Self-Assembled Monolayers for High-Performance Perovskite Solar Cells. *Angew. Chem., Int. Ed. Engl.* **2022**, *61* (51), e202213560.
- (12) Yao, Y.; Cheng, C.; Zhang, C.; Hu, H.; Wang, K.; De Wolf, S. Organic Hole-Transport Layers for Efficient, Stable, and Scalable Inverted Perovskite Solar Cells. *Adv. Mater.* **2022**, *34*, e2203794.
- (13) Chen, Q.; Wang, C.; Li, Y.; Chen, L. Interfacial Dipole in Organic and Perovskite Solar Cells. *J. Am. Chem. Soc.* **2020**, *142* (43), 18281–18292.
- (14) Paniagua, S. A.; Giordano, A. J.; Smith, O. L.; Barlow, S.; Li, H.; Armstrong, N. R.; Pemberton, J. E.; Bredas, J. L.; Ginger, D.; Marder, S. R. Phosphonic Acids for Interfacial Engineering of Transparent Conductive Oxides. *Chem. Rev.* **2016**, *116* (12), 7117–7158.
- (15) Azmi, R.; Ugur, E.; Seitkhan, A.; Aljamaan, F.; Subbiah, A. S.; Liu, J.; Harrison, G. T.; Nugraha, M. I.; Eswaran, M. K.; Babics, M.; Chen, Y.; Xu, F.; Allen, T. G.; Rehman, A. U.; Wang, C. L.; Anthopoulos, T. D.; Schwingenschlögl, U.; De Bastiani, M.; Aydin, E.; De Wolf, S. Damp Heat-Stable Perovskite Solar Cells with Tailored-Dimensionality 2D/3D Heterojunctions. *Science* **2022**, *376* (6588), 73–77.
- (16) Al-Ashouri, A.; Magomedov, A.; Roß, M.; Jošt, M.; Talaikis, M.; Chistiakova, G.; Bertram, T.; Márquez, J. A.; Köhnen, E.; Kasparavičius, E.; Levenco, S.; Gil-Escríg, L.; Hages, C. J.; Schlatmann, R.; Rech, B.; Malinauskas, T.; Unold, T.; Kaufmann, C. A.; Korte, L.; Niaura, G.; Getautis, V.; Albrecht, S. Conformal Monolayer Contacts with Lossless Interfaces for Perovskite Single Junction and Monolithic Tandem Solar Cells. *Energy Environ. Sci.* **2019**, *12* (11), 3356–3369.
- (17) Farag, A.; Feeney, T.; Hossain, I. M.; Schackmar, F.; Fassl, P.; Kuster, K.; Bauerle, R.; Ruiz-Preciado, M. A.; Hentschel, M.; Ritzer, D. B.; Diercks, A.; Li, Y.; Nejand, B. A.; Laufer, F.; Singh, R.; Starke, U.; Paetzold, U. W. Evaporated Self-Assembled Monolayer Hole Transport Layers: Lossless Interfaces in p-i-n Perovskite Solar Cells. *Adv. Energy Mater.* **2023**, *13* (8), 2203982.
- (18) Cassella, E. J.; Spooner, E. L. K.; Thornber, T.; O'Kane, M. E.; Catley, T. E.; Bishop, J. E.; Smith, J. A.; Game, O. S.; Lidzey, D. G. Gas-Assisted Spray Coating of Perovskite Solar Cells Incorporating Sprayed Self-Assembled Monolayers. *Adv. Sci.* **2022**, *9* (14), e2104848.
- (19) Gharibzadeh, S.; Fassl, P.; Hossain, I. M.; Rohrbeck, P.; Frericks, M.; Schmidt, M.; Duong, T.; Khan, M. R.; Abzieher, T.; Nejand, B. A.; Schackmar, F.; Almora, O.; Feeney, T.; Singh, R.; Fuchs, D.; Lemmer, U.; Hofmann, J. P.; Weber, S. A. L.; Paetzold, U. W. Two Birds with One Stone: Dual Grain-Boundary and Interface Passivation Enables > 22% Efficient Inverted Methylammonium-Free Perovskite Solar Cells. *Energy Environ. Sci.* **2021**, *14* (11), 5875–5893.
- (20) Ross, M.; Gil-Escríg, L.; Al-Ashouri, A.; Tockhorn, P.; Jost, M.; Rech, B.; Albrecht, S. Co-Evaporated p-i-n Perovskite Solar Cells beyond 20% Efficiency: Impact of Substrate Temperature and Hole-Transport Layer. *ACS Appl. Mater. Interfaces* **2020**, *12* (35), 39261–39272.
- (21) Aktas, E.; Phung, N.; Köbler, H.; González, D. A.; Méndez, M.; Kafedjiska, I.; Turren-Cruz, S.-H.; Wenisch, R.; Lauermann, I.; Abate, A.; Palomares, E. Understanding the Perovskite/Self-Assembled Selective Contact Interface for Ultra-Stable and Highly Efficient p-i-n Perovskite Solar Cells. *Energy Environ. Sci.* **2021**, *14* (7), 3976–3985.
- (22) Lin, Y.; Magomedov, A.; Firdaus, Y.; Kaltsas, D.; El-Labban, A.; Faber, H.; Naphade, D. R.; Yengel, E.; Zheng, X.; Yarali, E.; Chaturvedi, N.; Loganathan, K.; Gkeká, D.; AlShammari, S. H.; Bakr, O. M.; Laquai, F.; Tsetseris, L.; Getautis, V.; Anthopoulos, T. D. 18.4% Organic Solar Cells Using a High Ionization Energy Self-Assembled Monolayer as Hole-Extraction Interlayer. *ChemSusChem* **2021**, *14* (17), 3569–3578.
- (23) Lin, Y.; Zhang, Y.; Zhang, J.; Marcinkas, M.; Malinauskas, T.; Magomedov, A.; Nugraha, M. I.; Kaltsas, D.; Naphade, D. R.; Harrison, G. T.; El-Labban, A.; Barlow, S.; De Wolf, S.; Wang, E.; McCulloch, I.; Tsetseris, L.; Getautis, V.; Marder, S. R.; Anthopoulos, T. D. 18.9% Efficient Organic Solar Cells Based on n-Doped Bulk-Heterojunction and Halogen-Substituted Self-Assembled Monolayers as Hole Extracting Interlayers. *Adv. Energy Mater.* **2022**, *12*, 2202503.
- (24) Brinkmann, K. O.; Becker, T.; Zimmermann, F.; Kreusel, C.; Gahlmann, T.; Theisen, M.; Haeger, T.; Olthof, S.; Tuckmantel, C.; Gunster, M.; Maschwitz, T.; Gobelsmann, F.; Koch, C.; Hertel, D.; Caprioglio, P.; Pena-Camargo, F.; Perdigon-Toro, L.; Al-Ashouri, A.; Merten, L.; Hinderhofer, A.; Gomell, L.; Zhang, S.; Schreiber, F.; Albrecht, S.; Meerholz, K.; Neher, D.; Stolterfoht, M.; Riedl, T. Perovskite-Organic Tandem Solar Cells with Indium Oxide Interconnect. *Nature* **2022**, *604* (7905), 280–286.
- (25) Lin, R.; Wang, Y.; Lu, Q.; Tang, B.; Li, J.; Gao, H.; Gao, Y.; Li, H.; Ding, C.; Wen, J.; Wu, P.; Liu, C.; Zhao, S.; Xiao, K.; Liu, Z.; Ma, C.; Deng, Y.; Li, L.; Fan, F.; Tan, H. All-Perovskite Tandem Solar Cells with 3D/3D Bilayer Perovskite Heterojunction. *Nature* **2023**, *620* (7976), 994–1000.
- (26) Li, L.; Wang, Y.; Wang, X.; Lin, R.; Luo, X.; Liu, Z.; Zhou, K.; Xiong, S.; Bao, Q.; Chen, G.; Tian, Y.; Deng, Y.; Xiao, K.; Wu, J.; Saidaminov, M. I.; Lin, H.; Ma, C.-Q.; Zhao, Z.; Wu, Y.; Zhang, L.; Tan, H. Flexible All-Perovskite Tandem Solar Cells Approaching 25% Efficiency with Molecule-Bridged Hole-Selective Contact. *Nat. Energy* **2022**, *7* (8), 708–717.
- (27) Chiang, Y. H.; Frohma, K.; Salway, H.; Abfalterer, A.; Pan, L.; Roose, B.; Anaya, M.; Stranks, S. D. Vacuum-Deposited Wide-Bandgap Perovskite for All-Perovskite Tandem Solar Cells. *ACS Energy Lett.* **2023**, *8* (6), 2728–2737.
- (28) Chin, X. Y.; Turkay, D.; Steele, J. A.; Tabean, S.; Eswara, S.; Mensi, M.; Fiala, P.; Wolff, C. M.; Paracchino, A.; Artuk, K.; Jacobs, D.; Guesnay, Q.; Sahli, F.; Andreatta, G.; Boccard, M.; Jeangros, Q.; Ballif, C. Interface Passivation for 31.25%-Efficient Perovskite/Silicon Tandem Solar Cells. *Science* **2023**, *381* (6653), 59–63.
- (29) Mariotti, S.; Kohnen, E.; Scheler, F.; Sveinbjörnsson, K.; Zimmermann, L.; Piot, M.; Yang, F.; Li, B.; Warby, J.; Musienko, A.;

- Menzel, D.; Lang, F.; Kessler, S.; Levine, I.; Mantione, D.; Al-Ashouri, A.; Hartel, M. S.; Xu, K.; Cruz, A.; Kurpiers, J.; Wagner, P.; Kobler, H.; Li, J.; Magomedov, A.; Mecerreyres, D.; Unger, E.; Abate, A.; Stolterfoht, M.; Stannowski, B.; Schlatmann, R.; Korte, L.; Albrecht, S. Interface Engineering for High-Performance, Triple-Halide Perovskite-Silicon Tandem Solar Cells. *Science* **2023**, *381* (6653), 63–69.
- (30) Levine, I.; Al-Ashouri, A.; Musienko, A.; Hempel, H.; Magomedov, A.; Drevilkauskaitė, A.; Getautis, V.; Menzel, D.; Hinrichs, K.; Unold, T.; Albrecht, S.; Dittrich, T. Charge Transfer Rates and Electron Trapping at Buried Interfaces of Perovskite Solar Cells. *Joule* **2021**, *5* (11), 2915–2933.
- (31) Pitaro, M.; Alonso, J. S.; Di Mario, L.; Garcia Romero, D.; Tran, K.; Zaharia, T.; Johansson, M. B.; Johansson, E. M. J.; Loi, M. A. A Carbazole-Based Self-Assembled Monolayer as the Hole Transport Layer for Efficient and Stable $\text{Cs}_{0.25}\text{FA}_{0.75}\text{Sn}_{0.5}\text{Pb}_{0.5}\text{I}_3$ Solar Cells. *J. Mater. Chem. A* **2023**, *11* (22), 11755–11766.
- (32) Phung, N.; Verheijen, M.; Todanova, A.; Datta, K.; Verhage, M.; Al-Ashouri, A.; Kobler, H.; Li, X.; Abate, A.; Albrecht, S.; Creatore, M. Enhanced Self-Assembled Monolayer Surface Coverage by ALD NiO in p-i-n Perovskite Solar Cells. *ACS Appl. Mater. Interfaces* **2022**, *14* (1), 2166–2176.
- (33) Datta, K.; Wang, J.; Zhang, D.; Zardetto, V.; Remmerswaal, W. H. M.; Weijtens, C. H. L.; Wienk, M. M.; Janssen, R. A. J. Monolithic All-Perovskite Tandem Solar Cells with Minimized Optical and Energetic Losses. *Adv. Mater.* **2022**, *34* (11), e2110053.
- (34) Magomedov, A.; Al-Ashouri, A.; Kasparavičius, E.; Strazdaite, S.; Niaura, G.; Jošt, M.; Malinauskas, T.; Albrecht, S.; Getautis, V. Self-Assembled Hole Transporting Monolayer for Highly Efficient Perovskite Solar Cells. *Adv. Energy Mater.* **2018**, *8* (32), 1801892.
- (35) Mishima, R.; Hino, M.; Kanematsu, M.; Kishimoto, K.; Ishibashi, H.; Konishi, K.; Okamoto, S.; Irie, T.; Fujimoto, T.; Yoshida, W.; Uzu, H.; Adachi, D.; Yamamoto, K. 28.3% Efficient Perovskite-Silicon Tandem Solar Cells with Mixed Self-Assembled Monolayers. *Appl. Phys. Express* **2022**, *15* (7), 076503.
- (36) Kapil, G.; Bessho, T.; Sanehira, Y.; Sahamir, S. R.; Chen, M.; Baranwal, A. K.; Liu, D.; Sono, Y.; Hirotani, D.; Nomura, D.; Nishimura, K.; Kamarudin, M. A.; Shen, Q.; Segawa, H.; Hayase, S. Tin-Lead Perovskite Solar Cells Fabricated on Hole Selective Monolayers. *ACS Energy Lett.* **2022**, *7* (3), 966–974.
- (37) Deng, X.; Qi, F.; Li, F.; Wu, S.; Lin, F. R.; Zhang, Z.; Guan, Z.; Yang, Z.; Lee, C. S.; Jen, A. K. Co-assembled Monolayers as Hole-Selective Contact for High-Performance Inverted Perovskite Solar Cells with Optimized Recombination Loss and Long-Term Stability. *Angew. Chem., Int. Ed. Engl.* **2022**, *61* (30), e202203088.
- (38) Sun, J. J.; Shou, C. H.; Sun, J. S.; Wang, X. L.; Yang, Z. H.; Chen, Y.; Wu, J. R.; Yang, W. C.; Long, H. L.; Ying, Z. Q.; Yang, X.; Sheng, J.; Yan, B. J.; Ye, J. C. NiOx-Seeded Self-Assembled Monolayers as Highly Hole-Selective Passivating Contacts for Efficient Inverted Perovskite Solar Cells. *Solar RRL* **2021**, *5* (11), 2100663.
- (39) Alghamdi, A. R. M.; Yanagida, M.; Shirai, Y.; Andersson, G. G.; Miyano, K. Surface Passivation of Sputtered NiO_x Using a SAM Interface Layer to Enhance the Performance of Perovskite Solar Cells. *ACS Omega* **2022**, *7* (14), 12147–12157.
- (40) Mao, L.; Yang, T.; Zhang, H.; Shi, J.; Hu, Y.; Zeng, P.; Li, F.; Gong, J.; Fang, X.; Sun, Y.; Liu, X.; Du, J.; Han, A.; Zhang, L.; Liu, W.; Meng, F.; Cui, X.; Liu, Z.; Liu, M. Fully Textured, Production-Line Compatible Monolithic Perovskite/Silicon Tandem Solar Cells Approaching 29% Efficiency. *Adv. Mater.* **2022**, *34* (40), e2206193.
- (41) Chockalingam, M.; Darwish, N.; Le Saux, G.; Gooding, J. J. Importance of the indium tin oxide substrate on the quality of self-assembled monolayers formed from organophosphonic acids. *Langmuir* **2011**, *27* (6), 2545–2552.
- (42) Guo, R.; Wang, X.; Jia, X.; Guo, X.; Li, J.; Li, Z.; Sun, K.; Jiang, X.; Alvianto, E.; Shi, Z.; Schwartzkopf, M.; Müller-Buschbaum, P.; Hou, Y. Refining the Substrate Surface Morphology for Achieving Efficient Inverted Perovskite Solar Cells. *Adv. Energy Mater.* **2023**, *13*, 2302280.
- (43) Wu, M.; Li, X.; Ying, Z. Q.; Chen, Y.; Wang, X. L.; Zhang, M. L.; Su, S. Q.; Guo, X. C.; Sun, J. S.; Shou, C. H.; Yang, X.; Ye, J. C. Reconstruction of the Indium Tin Oxide Surface Enhances the Adsorption of High-Density Self-Assembled Monolayer for Perovskite/Silicon Tandem Solar Cells. *Ad. Funct. Mater.* **2023**, *33*, 2304708.
- (44) Aydin, E.; Troughton, J.; De Bastiani, M.; Ugur, E.; Sajjad, M.; Alzahrani, A.; Neophytou, M.; Schwingenschlögl, U.; Laquai, F.; Baran, D.; De Wolf, S. Room-Temperature-Sputtered Nanocrystalline Nickel Oxide as Hole Transport Layer for p-i-n Perovskite Solar Cells. *ACS Appl. Energy Mater.* **2018**, *1* (11), 6227–6233.
- (45) Boyd, C. C.; Shallcross, R. C.; Moot, T.; Kerner, R.; Bertoluzzi, L.; Onno, A.; Kavadiya, S.; Chosy, C.; Wolf, E. J.; Werner, J.; Raiford, J. A.; de Paula, C.; Palmstrom, A. F.; Yu, Z. J.; Berry, J. J.; Bent, S. F.; Holman, Z. C.; Luther, J. M.; Ratcliff, E. L.; Armstrong, N. R.; McGehee, M. D. Overcoming Redox Reactions at Perovskite-Nickel Oxide Interfaces to Boost Voltages in Perovskite Solar Cells. *Joule* **2020**, *4* (8), 1759–1775.
- (46) Lin, J.; Wang, Y.; Khaleed, A.; Syed, A. A.; He, Y.; Chan, C. C. S.; Li, Y.; Liu, K.; Li, G.; Wong, K. S.; Popovic, J.; Fan, J.; Ng, A. M. C.; Djuricic, A. B. Dual Surface Modifications of NiO_x /Perovskite Interface for Enhancement of Device Stability. *ACS Appl. Mater. Interfaces* **2023**, *15* (20), 24437–24447.
- (47) Yamaguchi, S.; Sato, A.; Ajiro, K.; Shiokawa, M.; Hashimoto, Y.; Maeda, T.; Sugiyama, M.; Gotanda, T.; Marumoto, K. Performance Improvement Mechanisms of Perovskite Solar Cells by Modification of NiO_x Hole-Selective Contacts with Self-Assembled-Monolayers. *Sol. Energy Mater. Sol. Cells* **2023**, *258*, 112428.
- (48) Zheng, X.; Song, Z.; Chen, Z.; Bista, S. S.; Gui, P.; Shrestha, N.; Chen, C.; Li, C.; Yin, X.; Awni, R. A.; Lei, H.; Tao, C.; Ellingson, R. J.; Yan, Y.; Fang, G. Interface Modification of Sputtered NiO_x as the Hole-Transporting Layer for Efficient Inverted Planar Perovskite Solar Cells. *J. Mater. Chem. C* **2020**, *8* (6), 1972–1980.
- (49) Phung, N.; Zhang, D.; van Helvoort, C.; Verhage, M.; Verheijen, M.; Zardetto, V.; Bens, F.; Weijtens, C. H. L.; Geerligs, L. J.; Kessels, W. M. M.; Macco, B.; Creatore, M. Atomic Layer Deposition of NiO Applied in a Monolithic Perovskite/PERC Tandem Cell. *Sol. Energy Mater. Sol. Cells* **2023**, *261*, 112498.
- (50) Maryon, O. O.; Efaw, C. M.; DelRio, F. W.; Graugnard, E.; Hurley, M. F.; Davis, P. H. Co-localizing Kelvin Probe Force Microscopy with Other Microscopies and Spectroscopies: Selected Applications in Corrosion Characterization of Alloys. *J. Vis. Exp.* **2022**, No. 184, e64102.
- (51) Yoshitake, M. *Work Function and Band Alignment of Electrode Materials*; Springer Tokyo: Japan, 2021.
- (52) Walsh, A.; Catlow, C. R. A. Structure, Stability and Work Functions of the Low Index Surfaces of Pure Indium Oxide and Sn-doped Indium Oxide (ITO) from Density Functional Theory. *J. Mater. Chem.* **2010**, *20* (46), 10438–10444.
- (53) Tasker, P. W. The Stability of Ionic Crystal Surfaces. *J. Phys. C: Solid State Phys.* **1979**, *12* (22), 4977–4984.
- (54) Hubmann, A. H.; Dietz, D.; Brotz, J.; Klein, A. Interface Behaviour and Work Function Modification of Self-Assembled Monolayers on Sn-Doped In_2O_3 . *Surfaces* **2019**, *2* (2), 241–256.
- (55) Hohmann, M. V.; Agoston, P.; Wachau, A.; Bayer, T. J.; Brotz, J.; Albe, K.; Klein, A. Orientation Dependent Ionization Potential of In_2O_3 : A Natural Source for Inhomogeneous Barrier Formation at Electrode Interfaces in Organic Electronics. *J. Phys.: Condens. Matter* **2011**, *23* (33), 334203.
- (56) Whitten, J. E. Ultraviolet Photoelectron Spectroscopy: Practical Aspects and Best Practices. *Appl. Surf. Sci.* **2023**, *13*, 100384.